Chemical Engineering Journal 371 (2019) 666–678

Contents lists available at ScienceDirect

Chemical Engineering Journal

journal homepage: www.elsevier.com/locate/cej

Study on removal of elemental mercury over MoO_3-CeO_2/cylindrical activated coke in the presence of SO_2 by Hg-temperature-programmed desorption

Miao Liu[a,b], Caiting Li[a,b,*], Qiang Zeng[a,b], Xueyu Du[a,b], Lei Gao[a,b], Shanhong Li[a,b], Yunbo Zhai[a,b]

[a] College of Environmental Science and Engineering, Hunan University, Changsha 410082, PR China
[b] Key Laboratory of Environmental Biology and Pollution Control (Hunan University), Ministry of Education, Changsha 410082, PR China

HIGHLIGHTS

- MoCe0.5/AC exhibited high Hg^0 removal efficiency at 120 °C.
- The adsorption mercury species were identified by Hg-TPD technique.
- The mechanism for Hg^0 removal was reasonably speculated.
- The mechanism on high SO_2 resistance of MoCe0.5/AC was investigated.

GRAPHICAL ABSTRACT

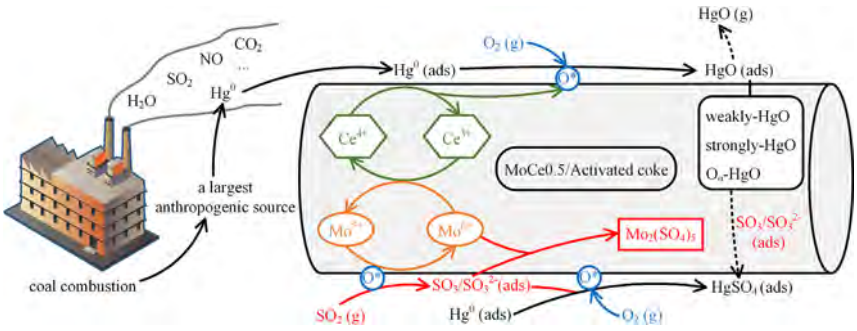

ARTICLE INFO

Keywords:
Hg^0 adsorption
Activated coke
MoO_3-CeO_2
Sulfur tolerance
Hg-TPD

ABSTRACT

MoO_3-CeO_2/cylindrical activated coke samples (MoCeY/AC) synthesized by an impregnation method were employed to investigate elemental mercury (Hg^0) removal at 60–210 °C from simulated flue gas without HCl. MoCe0.5/AC with an optimal Mo/Ce molar ratio of 0.5 exhibited an excellent Hg^0 removal efficiency (94.74%) at 120 °C, as well as good stability and prominent resistance to SO_2 and H_2O. The physicochemical property of the samples and the Hg^0 removal mechanism were discussed by ICP-AES, SEM, EDX, BET, XRD, H_2-TPR, XPS and Hg-TPD. The results of characterizations showed that MoCe0.5/AC possessed the special petal-like outer microstructure, large BET surface area, well-dispersed metal oxides and high reducibility, which was conducive for Hg^0 removal. Furthermore, the synergistic effect between Mo^{6+} and Ce^{3+} was favorable to the high Hg^0 removal performance by providing high valence Ce. According to the Hg-TPD tests, the chemisorption of Hg^0 was a major approach for Hg^0 removal, while physisorption and catalytic oxidation were just accounted for a tiny fraction. Moreover, the chemisorbed mercury could be validly distinguished into weakly-HgO, strongly-HgO, O_α-HgO and $HgSO_4$ (when SO_2 was added). Compared with raw AC, MoCe0.5/AC could enhance the Hg^0 oxidation performance and produce O_α-HgO during the Hg^0 removal process. In addition, the possible reason for the high SO_2 tolerance of MoCe0.5/AC was examined: (i) the preferential combination between sulfate and MoO_3 could protect CeO_2 for Hg^0 removal; (ii) SO_2 could contribute to the formations of weakly-HgO and $HgSO_4$. Finally, the regenerability of MoCe0.5/AC was also discussed.

* Corresponding author at: College of Environmental Science and Engineering, Hunan University, Changsha 410082, PR China.
E-mail address: ctli@hnu.edu.cn (C. Li).

https://doi.org/10.1016/j.cej.2019.04.088
Received 23 February 2019; Received in revised form 11 April 2019; Accepted 12 April 2019
Available online 13 April 2019
1385-8947/

1. Introduction

The release of mercury has become a global concern for its toxicity, long-range transport and bioaccumulation in the food chain and the environment [1]. To protect the creature health and the environment from worldwide anthropogenic mercury releases, 128 countries have signed the Minamata Convention on Mercury in 2013 [2]. Therein, coal combustion, a major energy source on this planet, is considered as one of the largest contributors to anthropogenic mercury releases [3–5]. Mercury in coal-fired flue gas generally exists in the form of particulate-bound mercury (Hg^P), oxidized mercury (Hg^{2+}) and elemental mercury (Hg^0) [6]. Hg^P and Hg^{2+} can be effectively controlled by existing air pollution control devices, whereas Hg^0 cannot because of its high volatility and low solubility [7]. Hence, developing effective and economical technology for removing Hg^0 from flue gas is of significance in practical industry.

Various technologies have been developed for Hg^0 removal, including adsorption [8], catalytic oxidation [9,10] and photochemical oxidation [11]. Among them, adsorption is the most common one in industry, especially the activated carbon injection (ACI) technology [12]. However, activated carbon as traditional mercury sorbent has limitations for its high-cost, poor efficiency and low regeneration rate [13]. Therefore, new sorbents have been explored for Hg^0 removal on a fixed-bed reactor, including activated coke [14,15], biochar [8], graphene [16] and others [17–19]. Hereinto, activated coke (AC), a porous carbon-based adsorbent with partly activation, is regarded as a promising one. The feasibility comes from its abundant surface functional groups, higher mechanical strength, better regeneration performance and higher economic benefits [20,21]. Nevertheless, Hg^0 removal performance of raw AC is commonly confined by its limited surface active sites and the unavoidable components in realistic coal-fired flue gas [22,23]. In particular, water vapor always inhibits the Hg^0 removal for the competitive adsorption with Hg^0 [24]. Moreover, SO_2 could not only compete with Hg^0 for the surface active sites but also restrain the Hg^0 oxidation by reacting with active components [25]. Thus further efforts are needed to improve the H_2O and SO_2 resistance and Hg^0 removal efficiency of activated coke sorbent simultaneously.

It is reported that modification of raw AC is conducive to effective removal of SO_2 [21], NO_x [26], Hg^0 [14] and VOCs [27]. In the previous studies, to enhance the Hg^0 removal performance, the raw AC has been suitable chemical modified by acid [23,28], metal oxides [15,22] or/and halogen [29]. In view of the secondary contamination and the high price by acid and halogen [30,31], the one modified by metal oxides has received more attention due to the low-cost and environmental friendliness. Because of their various valence states and high chemical stability, transition metal oxides such as CuO [15], CeO_2 [22], CoO_3-CeO_2 [13], La_2O_3-CeO_2 [14], MnO_x-FeO_x [27] and others have been widely recognized as promising materials for Hg^0 removal [32]. However, as another crucial parameter for industrial application, the SO_2 tolerance of the modified AC in the previous studies is desired to improve, and the mechanism is fuzzy.

The CeO_2-based catalyst, with unique redox couple Ce^{3+}/Ce^{4+} and high catalytic activity, is well-established use in various heterogeneous reactions and has a great application prospect [33,34]. However, the SO_2 tolerance of CeO_2 modified AC sorbents were not good enough [20,22]. According to reports [35,36], SO_2 could easily react with CeO_2 and produce $Ce_2(SO_4)_3$ and/or $Ce(SO_4)_2$, which would interdict the shift between Ce^{4+} and Ce^{3+}, thus restrain the Hg^0 removal. In contrast, several studies have revealed that using MoO_3 as a promoter or stabilizer for materials would acquire higher catalytic activity and stability, including the SO_2 resistance [24,37–39]. For example, Li et al. [24] reported that both the Hg^0 oxidation activity and the SO_2 tolerance were enhanced after Mo had been added into CoO_x/Ti-Ce catalyst. Kwon et al. [38] also confirmed that the SO_2 resistance of Mo-doped VO_x/TiO_2 catalyst was increased, as the reaction between V = O and SO_2 was inhibited by high Mo^{6+}/Mo^{5+} ratio. Hence, using bimetallic Mo and Ce to modified AC (MoCeY/AC) might inherit the high Hg^0 removal performance of CeO_2 and the SO_2 tolerance of MoO_3 simultaneously. Moreover, to our knowledge, using MoCeY/AC for the removal of Hg^0 in the presence of SO_2 has rarely been reported.

Herein, MoCeY/AC samples synthesized by the impregnation method were studied for the Hg^0 removal in a fixed-bed reaction system. The structure and surface property of the samples were characterized using SEM, EDX, BET, XRD, H_2-TPR and XPS. Some influence factors, such as Mo/Ce molar ratio, reaction temperature and flue gas components (O_2, NO, SO_2 and H_2O), were investigated. Moreover, the possible Hg^0 removal mechanism was reasonably deduced by Hg-temperature-programmed desorption (Hg-TPD) technique. As we all know, Hg-TPD is an efficient method to simultaneous identify multiple adsorbed mercury compounds clearly and without interference [40,41]. Because the adsorbed mercury species, owning different interaction force between the mercury and the active sites, can be decomposed into Hg^0 at their characteristic decomposition temperature [16,42]. Besides, the reasons for the high SO_2 resistance and regeneration performance of the MoCe0.5/AC were also discussed, which has been few reported on the modified AC sorbents before.

2. Experiment

2.1. Samples preparation

The samples were synthesized by the impregnation method. Cylinder commercial activated coke granule (AC, diameter = 5 mm, length = 5–8 mm, Alxa League Ke'xing Carbon Industry, China) was served as the support. The virgin AC was repeatedly washed by deionized (DI) water, and then was desiccated at 105 °C for 12 h in air. Mo/AC was prepared by impregnating AC with a calculated amount of ammonium molybdate ($(NH_4)_6Mo_7O_{24}{\cdot}4H_2O$) aqueous solution at room temperature for 24 h, then dried at 105 °C for 12 h in air, and followed by calcining at 500 °C for 4 h under pure N_2 flow. Similarly, Ce/AC was obtained using the same method, while the precursor was replaced by cerium nitrate ($Ce(NO_3)_3{\cdot}6H_2O$). MoCeY/AC samples with different Mo/Ce molar ratio (denoted as Y = 0.2, 0.5, 1, 1.5) were made by impregnating Mo/AC with cerium nitrate aqueous solution for 24 h, then desiccated at 105 °C for 12 h in air and calcined at 500 °C for 4 h in N_2. Considering the effectivity and economy, the total metal mass percentage (Mo and/or Ce) on modified AC sample was selected as 5 wt %.

2.2. Samples characterization

The metal contents of modified samples were characterized by an Inductively Coupled Plasma-Atomic Emission Spectrometry (ICP-AES, SPECTRO BLUE SOP, Germany).

The surface morphology of materials was analyzed by the scanning electron microscope (SEM, TESCAN MIRA3 LMU, China), and the energy-dispersive X-ray spectroscopy (EDX, Oxford X-Max20 EDX Detector, UK) was utilized to local analysis the elemental composition at certain part of sample.

The Brunauer-Emmett-Teller (BET) specific surface area and total pore volume of the materials were obtained using a Quadrasorb SI-3MP (USA) instrument by N_2 adsorption at 77 K. The mesopore volume and micropore volume was determined by Barrett–Joyner–Halenda model and t-plot theory, respectively.

The X-ray diffraction (XRD) patterns were performed on a Riguku D/Max 2550 (Rigaku Corporation, Japan) diffractometer which operated at 40 kV and 250 mA using Cu Kα radiation.

The H_2-temperature-programmed reduction (H_2-TPR) was carried out on an AutoChem 2920 (China) automated adsorption analyzer equipped with a TCD detector. All of the tested samples were pretreated under N_2 flow at 300 °C for 30 min.

The X-ray photoelectron spectroscopy (XPS) measurements were

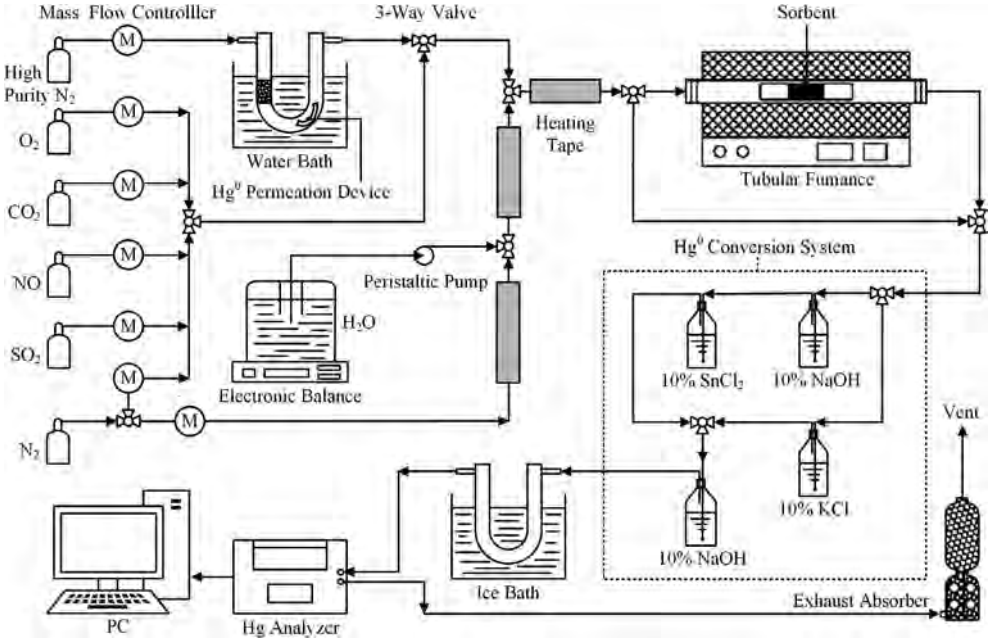

Fig. 1. Schematic diagram of the experimental setup.

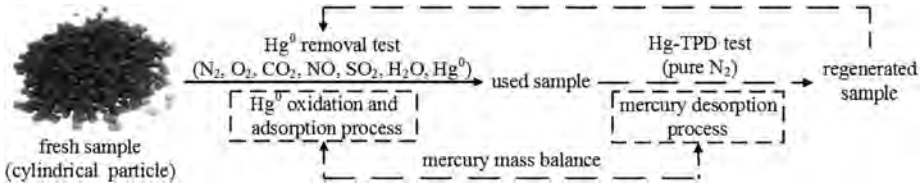

Fig. 2. Schematic diagram of the experimental design.

carried out on a Thermo K-Alpha 1063 spectrometer (Thermo Fisher Scientific, UK) while calibrated by the C 1s binding energy (BE) value of 284.6 eV. A spent MoCe0.5/AC sample treated after 52 h of Hg^0 removal under 6% O_2, 400 ppm of SO_2 (when used) and balanced by N_2 with a total flow rate of 500 mL/min at 120 °C.

2.3. Performance tests

Hg^0 oxidation and removal performance of the samples were evaluated in a fixed-bed quartz reactor (inner diameter = 52 mm, length = 870 mm), and the reaction temperature was controlled by a temperature controller. As shown in Fig. 1, the conventional gas components, such as N_2, O_2, CO_2, NO and SO_2, were offered by cylinders and exactly controlled by mass flow controllers (MFC). In addition, 8 vol% H_2O vapor was introduced using a peristaltic pump and evaporated with a heating tape. Hg^0 vapor was provided by a heated mercury permeation tube (VICI Metronics, USA) with 100 mL/min high purity N_2 (99.999%) as the carrier gas, and the concentration of Hg^0 was measured by online mercury analyzer (LUMEX RA-915 M, Russia). However, the RA-915 M analyzer could only measure the concentration of Hg^0, such as the inlet Hg^0 concentration (Hg^0_{in}) and the outlet Hg^0 concentration (Hg^0_{out}). Hence, a mercury speciation conversion system was added to calculate the outlet Hg^{2+} concentration (Hg^{2+}_{out}) and identify the Hg^0 oxidation performance. Within the conversion system, 10% KCl solution could capture Hg^{2+} for Hg^0 measurement, and 10% $SnCl_2$ solution could reduce Hg^{2+} to Hg^0 for outlet total Hg^0 measurement (Hg^T_{out}). The difference of the Hg^0 concentration between them was calculated as Hg^{2+}_{out}. Besides, 10% NaOH solution was set to remove acid gas, which could react with $SnCl_2$ solution and corrode the detection cell of the mercury analyzer. From the above, the Hg^0 removal efficiency (E_{rem}), Hg^0 oxidation efficiency (E_{oxi}) and Hg^0 adsorption efficiency (E_{ads}, including physisorption and chemisorption) were defined in Eqs. (1)–(3):

$$E_{rem}(\%) = \frac{Hg^0_{in} - Hg^0_{out}}{Hg^0_{in}} \times 100\% \quad (1)$$

$$E_{oxi}(\%) = \frac{Hg^{2+}_{out}}{Hg^0_{in}} \times 100\% = \frac{Hg^T_{out} - Hg^0_{out}}{Hg^0_{in}} \times 100\% \quad (2)$$

$$E_{ads}(\%) = E_{rem} - E_{oxi} \quad (3)$$

Schematic diagram of the experimental design was showed in Fig. 2, and the corresponding reaction conditions were explained as follow. The total gas flow rate during the whole experiment was adjusted at 500 mL/min. For the Hg^0 removal test, 20 g fresh sample was employed to remove 100 μg/m^3 Hg^0 for 3 h, giving a gas hourly space velocity (GHSV) of 2000 h^{-1}. To discuss the effects of Mo/Ce molar ratio and reaction temperature, the gas component was 6% O_2 + N_2 and the range of temperature was 60–210 °C. The effects of gas components were explored by changing the contents of O_2, NO, SO_2 and H_2O.

However, for the Hg-TPD test, the content of adsorption mercury over the used sorbents should be increased to reduce the experimental errors. Thus, the reaction conditions of Hg^0 removal before the Hg-TPD test were changed as follows: 10 g fresh sample was employed to remove 200 μg/m^3 Hg^0 for 5 h under 400 ppm of SO_2 (when used), 6% O_2 (when used) and balanced N_2 flow, corresponding to the GHSV of 4000 h^{-1}. Then, the resultant sorbents from Hg^0 removal test were examined in the Hg-TPD test. The temperature of Hg-TPD test was maintained at 150 °C in the initial 10 min to detect physically adsorbed Hg^0 [42], and then was warmed up to 700 °C with 10 °C/min heating rate to decompose the chemisorbed mercury species into Hg^0. Meanwhile, the Hg^0 was carried out by 500 mL/min pure N_2 flow, and the Hg-TPD curve appeared on the online mercury measurement system. Theoretically, the mass of Hg^0 adsorption (Q_{ads}, μg) during the Hg^0

removal test should equal to that of Hg^0 desorption (Q_D, μg) from Hg-TPD test. Moreover, the difference between the mass of Hg^0 removal (Q_R, μg) and Hg^0 oxidation (Q_{oxi}, μg) was equivalent to Q_{ads}. Therefore, the mercury mass balance ratio (B_{Hg}, %) could be calculated by the following formula:

$$B_{Hg} = \frac{Q_D}{Q_R - Q_{oxi}} \times 100\% = \frac{\int_{t_1'}^{t_2'} Hg_{TPD}^0 f dt}{\int_{t_1}^{t_2} (Hg_{in}^0 - Hg_{out}^0) f dt - E_{oxi} \int_{t_1}^{t_2} Hg_{in}^0 f dt} \times 100\% \quad (4)$$

where t_1 and t_2 present the initial and end time of the Hg^0 removal test (min), respectively; t_1' and t_2' for decomposition process. Hg_{TPD}^0 represents the outlet Hg^0 concentration of Hg-TPD test. f is the total flow rate constant as 500 mL/min. The Hg^0 oxidation during the Hg^0 removal test is considered stable.

After calculation, the B_{Hg} for the Hg^0 removal and desorption processes was close to 100%, meaning that almost all of the adsorbed mercury had been decomposed from the used sample. Therefore, the Hg-TPD test was considered as the effective process for sorbent regeneration [16]. Besides, the effects of regeneration times and SO_2 for the regeneration performance were also researched.

2.4. Quality assurance and quality control

For each test, the desired Hg_{in}^0 had been stabilized for at least 1 h and Hg_{out}^0 was recorded after the variation of Hg^0 concentration less than 5% for longer than 1 h. All of the tests were carried out three or more replicates to reproduce the results and reduce experimental error, and a blank test was performed to avoid any influence of the reactor. Besides, the error bars in the figures represented the standard deviation from the mean of the series of experiments at each condition. The insignificant deviations might owe the fluctuation of inlet Hg^0 concentration and sorbent bed reaction temperature [19].

3. Results and discussion

3.1. Structural characterization and redox properties

3.1.1. ICP-AES

The contents of molybdenum and ceria over the modified samples and the Mo/Ce molar ratio were obtained by ICP-AES. As demonstrated in Table 1, the practical metal loading value was slightly lower than the nominal one, which might be ascribed to the loss of molybdenum precursor and ceria precursor during the preparation [43]. However, the actual Mo/Ce molar ratio was nearly equivalent to the theoretical value, displaying that the preparation method was feasible.

3.1.2. SEM and EDX

The SEM images of as-prepared samples were presented in Fig. 3(a)–(g). Compared with the smooth surface of raw AC, the surface of Mo/AC possessed the circular-plate-like morphology and its agglomeration, while little granules were obtained over the Ce/AC. Particularly, a well-dispersed spherical morphology with petal-like outer appeared over the MoCe0.5/AC, which might be favorable for Hg^0 capture by contributing a vast of active sites and high BET surface area [27]. With continued increase of Mo, the surface morphology of MoCe1/AC and MoCe1.5/AC was transformed into square-plate-like form, even agglomerated over MoCe1.5/AC. Moreover, the EDX was used to rough detect the elemental composition of the specific morphology on MoCe0.5/AC, where the detecting point was signed on Fig. 3(e) as “Spectrum”. For the result of EDX (Fig. 3(h)), the Mo/Ce atomic ratio of the specific morphology on MoCe0.5/AC was 1.79, which was triple more than that of the whole MoCe0.5/AC as 0.52 (Table 1). These results indicated that the mainly metal of the agglomeration on MoCe0.5/AC was Mo, namely MoO_x was easier to agglomerate than CeO_x.

Table 1
The content of metal in samples obtained by ICP-AES.

Sample	Mo content (wt%)		Ce content (wt%)		Mo/Ce molar ratio	
	Nominal	Actual	Nominal	Actual	Nominal	Actual
Mo/AC	5.00	3.46	–	–	–	–
Ce/AC	–	–	5.00	4.50	–	–
MoCe0.2/AC	0.60	0.44	4.40	4.07	0.20	0.16
MoCe0.5/AC	1.28	1.11	3.72	3.09	0.50	0.52
MoCe1/AC	2.03	1.72	2.97	2.39	1.00	1.05
MoCe1.5/AC	2.53	1.96	2.47	1.95	1.50	1.47

3.1.3. BET

The BET results of the different samples were summarized in Table 2. For MoCeY/AC sample, when the content of loaded Mo was increased, both of the BET surface area and the content of micropore were reduced. In addition, the two counterparts of Mo/AC sharply decreased to 42.04 m^2/g and 42.89%, which were much lower than AC. In addition, the reduction of the micropore was also described in Fig. 4, and the pore size distribution of the different samples was approximately 0.7 nm and 4 nm. These results suggested that the easily agglomerating MoO_3 could reduce the BET surface area by blockade the partial pores. However, MoCe0.2/AC and MoCe0.5/AC showed the superior BET surface area of 245.03 m^2/g and 223.43 m^2/g, even higher than Ce/AC. It is probable the synergistic effect between Mo and Ce oxide species was beneficial to a larger BET surface area. It is a widely held view that the larger BET surface area of the sorbent, the more active sites and larger adsorbed interface it possessed, which was conducive for Hg^0 removal [44]. Thus, it was necessary to investigate an appropriate Mo/Ce molar ratio for high Hg^0 removal performance.

3.1.4. XRD

The XRD patterns of AC and modified samples were shown in Fig. 5. Two typical AC peaks (2θ = 26.68° and 44.50°, PDF-ICDD 25-0284) were detected over all of the samples. However, the weakened intensity of the AC peaks for the modified samples might reveal an interaction between metal oxides and carbon [14], which was also observed in SEM and BET. The diffraction peaks at 2θ = 26.06°, 28.84°, 36.98° and 53.56° in Mo/AC were assigned to MoO_3 (PDF-ICDD 65-7675), and the peaks at 2θ = 28.62°, 33.05°, 47.51° and 56.33° in Ce/AC were attributed to CeO_2 (PDF-ICDD 65-5923). In addition, both of MoO_3 (2θ = 28.84°) and CeO_2 diffraction peaks (2θ = 47.51° and 56.33°) existed in the MoCeY/AC. Furthermore, the intensity of the CeO_2 peaks was decreased and even disappeared with the gradually falling CeO_2 content, which conformed to the monolayer dispersion theory [45].

3.1.5. H_2-TPR

Reducibility of the different samples was investigated by H_2-TPR (Fig. 6). For the AC, the peak at 530 °C could be proposed to the reduction of surface oxygen species, and the peak at 672 °C accorded with the carbon gasification which also appeared in the modified samples [46]. Mo/AC exhibits two new reduction peaks, the peak centered at 546 °C represented the reduction of MoO_3 to MoO_2, while the 768 °C one corresponded to the reduction of MoO_2 to Mo metal [47]. For the Ce/AC, the reduction peak at 563 °C could be attributed to the reduction of surface Ce^{4+} to Ce^{3+}, and the peak at 734 °C was assigned to the bulk oxygen [28]. However, the reduction peaks centering at 553 °C and 720 °C of MoCe0.5/AC were hard to separate furtherly. The former one might be due to the co-reduction of MoO_3 and surface Ce^{4+}, while the latter one ascribed to the co-reduction of MoO_2 and bulk oxygen. The reduction peaks shifted to lower temperature indicate the higher reducibility MoCe0.5/AC owns, which caused by the mobility of active oxygen species enhanced from the interaction between Mo and Ce oxides [48].

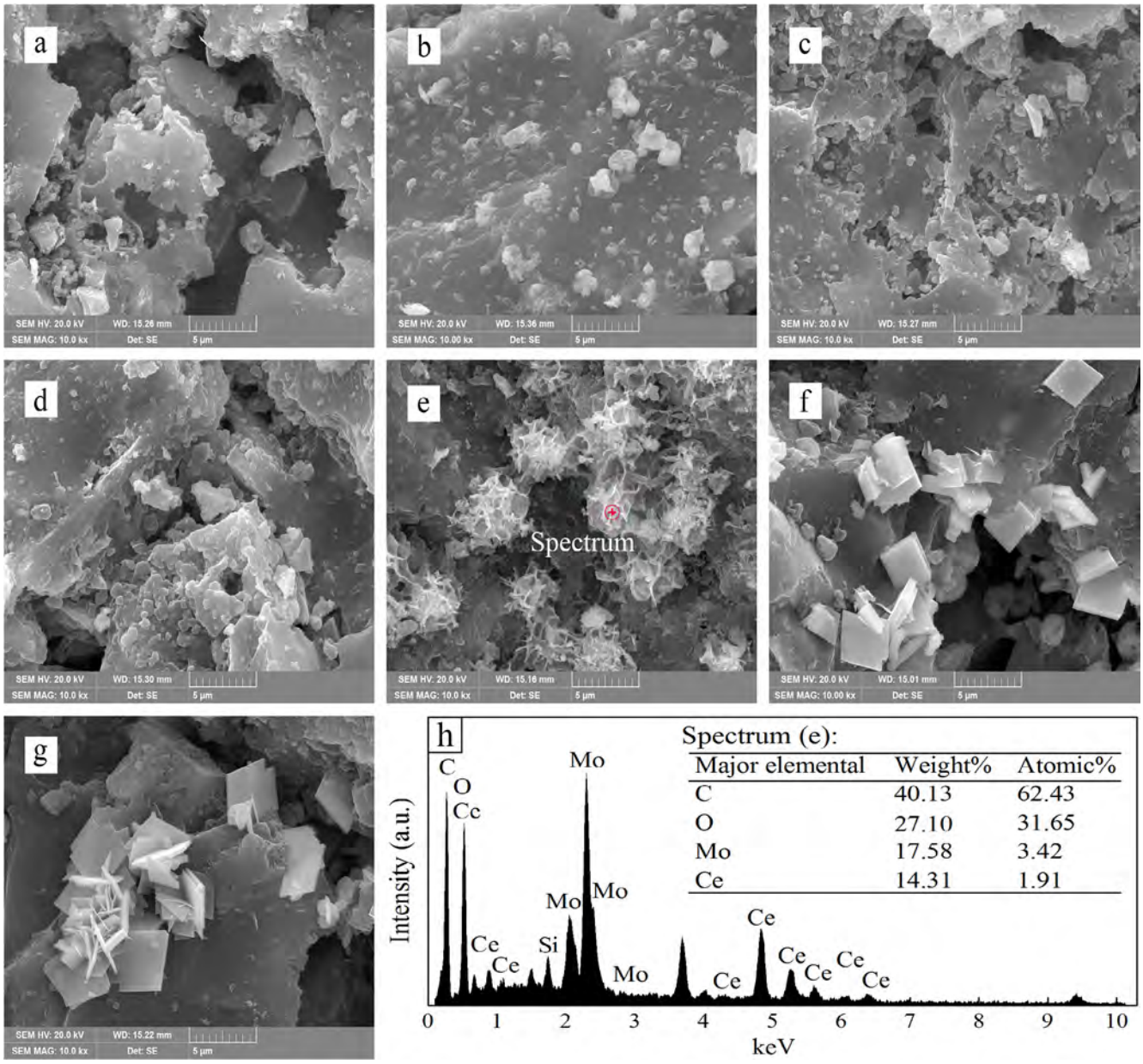

Fig. 3. (a)–(g) SEM images (×10,000), (a) AC, (b) Mo/AC, (c) Ce/AC, (d) MoCe0.2/AC, (e) MoCe0.5/AC, (f) MoCe1/AC, (g) MoCe1.5/AC; (h) EDX image of the MoCe0.5/AC.

Table 2
BET surface and pore parameters of the different samples.

Sample	BET surface area (m^2/g)	Average diameter (nm)	Total pore volume ($\times 10^{-2} cm^3/g$)	Pore volume distribution (%)	
				Micropore	Mesopore
AC	96.52	2.468	5.954	67.25	32.75
Mo/AC	42.04	3.635	3.821	42.89	57.01
Ce/AC	183.29	2.027	9.290	81.91	18.19
MoCe0.2/AC	245.03	1.800	11.02	88.18	11.82
MoCe0.5/AC	223.43	1.913	10.68	84.08	15.92
MoCe1/AC	176.78	2.040	9.133	80.42	19.58
MoCe1.5/AC	154.59	2.067	7.745	81.70	18.30
S-MoCe0.5/AC	200.12	2.018	10.10	79.63	20.37
OS-MoCe0.5/AC	128.59	2.200	7.075	73.48	26.52

Note: "S-MoCe0.5/AC" was MoCe0.5/AC pretreated by 400 ppm SO_2 + N_2 with 500 mL/min flow rate at 120 °C for 3 h; "OS-MoCe0.5/AC" was pretreated by 400 ppm SO_2 + 6% O_2 + N_2.

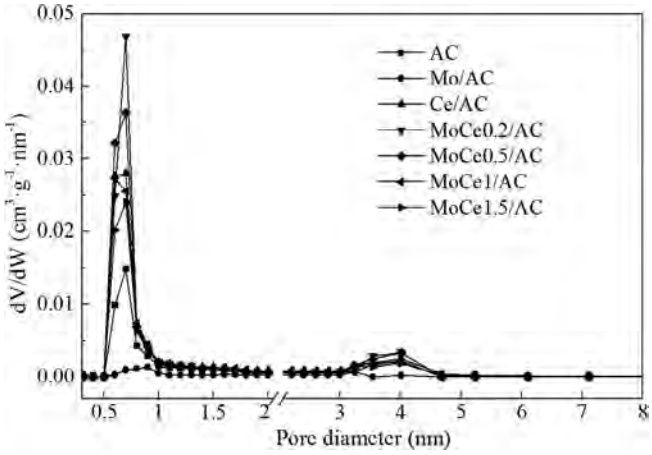

Fig. 4. The pore size distribution curves of the different samples.

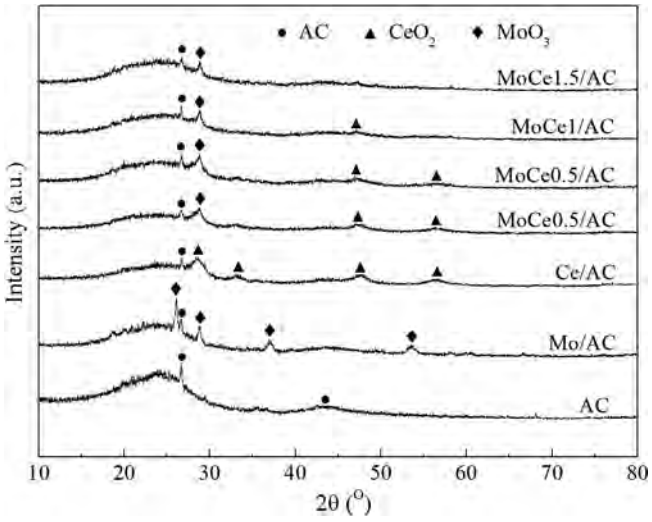

Fig. 5. XRD patterns of various samples.

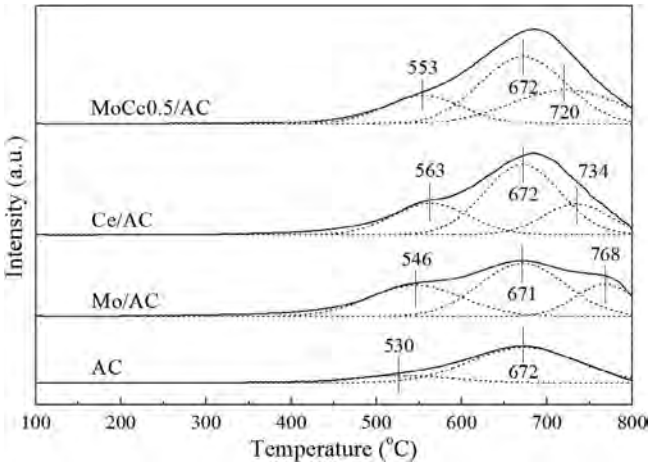

Fig. 6. H_2-TPR profiles of fresh AC, Mo/AC, Ce/AC and MoCe0.5/AC.

3.2. Sample performance test

The Hg^0 removal performance of various samples at 60–210 °C was investigated. As shown in Fig. 7, E_{rem} over all of the samples were obviously improved with rising of the reaction temperature from 60 °C to 120 °C. It might be a result of that more kinetic energy was provided by the higher temperature, which was beneficial to Hg^0 oxidation and adsorption [49]. However, E_{rem} reduced with continuously increasing of the temperature to 210 °C. The possible reason was that the physisorption of Hg^0 which combined with the surface of sorbent by weak wan der Waals forces was inhibited as the thermal energy enhanced, thereby the following Hg^0 oxidation and chemisorption were suppressed as well [15,29].

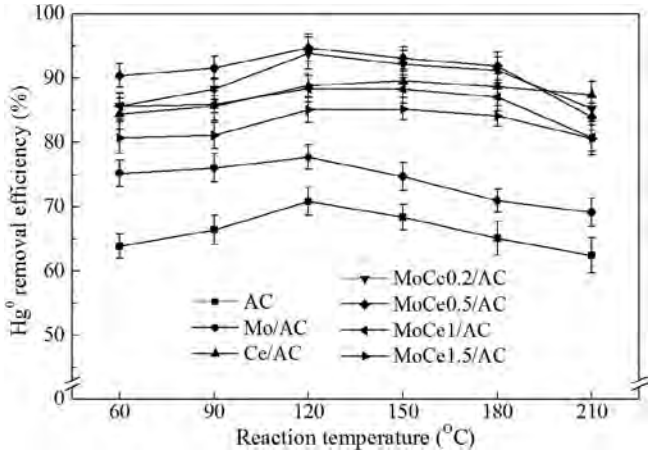

Fig. 7. Removal of Hg^0 over various samples. (Note: reaction time 3 h, 100 μg/m^3 Hg^0, 6% O_2, 20 g sample, GHSV 2000 h^{-1}).

Under the given temperature, the order of Hg^0 removal activity for different samples was similar to that of the BET surface area (Table 2), deducing that the BET surface area might play a role in the Hg^0 removal. However, it was not exactly the same. For example, Mo/AC with the lowest BET surface area had higher E_{rem} than AC. These results revealed that other factors, such as the microstructure and the Mo/Ce molar ratio, could influence Hg^0 removal performance of sample as well. Specifically, E_{rem} over MoCeY/AC samples firstly enhanced and then reduced as increasing the Mo/Ce molar ratio, and MoCe0.5/AC exhibited the highest E_{rem} reaching 94.74% at 120 °C.

From the above, the optimum sample MoCe0.5/AC possessed the special microstructure (Fig. 3(e)), large BET surface area (Table 2), well-dispersed metal oxides (Fig. 5) and high reducibility (Fig. 6), which was supported by the results of SEM, BET, XRD and H_2-TPR. These superior physicochemical characteristics could provide abundant active sites and large interface for Hg^0 adsorption, thus revealed the high Hg^0 removal performance [27,50]. Moreover, the performance of MoCe0.5/AC and MoCe0.2/AC was higher than that of Mo/AC and Ce/AC, implying that the synergistic effect between Mo and Ce oxide species was beneficial to Hg^0 removal. On the one hand, coexistence of Mo and Ce oxides could improve the microstructure and BET surface area. On the other hand, the metal oxides could reveal a higher reducibility and a large amount of surface active oxygen for Hg^0 removal. The mechanism of Hg^0 removal over MoCe0.5/AC should be further evidenced by mercury speciation conversion system, XPS, Hg-TPD and other else as follows.

3.3. Effects of gas components

Effects of gas components on Hg^0 oxidation and adsorption over MoCe0.5/AC were summarized in Fig. 8, in which simulated flue gas (SFG) was comprised by 6% O_2, 12% CO_2, 350 ppm of NO and 400 ppm of SO_2 balanced in N_2. The error bars in Fig. 8 represented the standard deviation from the mean of E_{oxi} and E_{ads}, respectively. Overall, the Hg^0 oxidation efficiency of MoCe0.5/AC was less than 10% whatever the reaction gas components were. Thus, Hg^0 adsorption was the critical factor for Hg^0 removal.

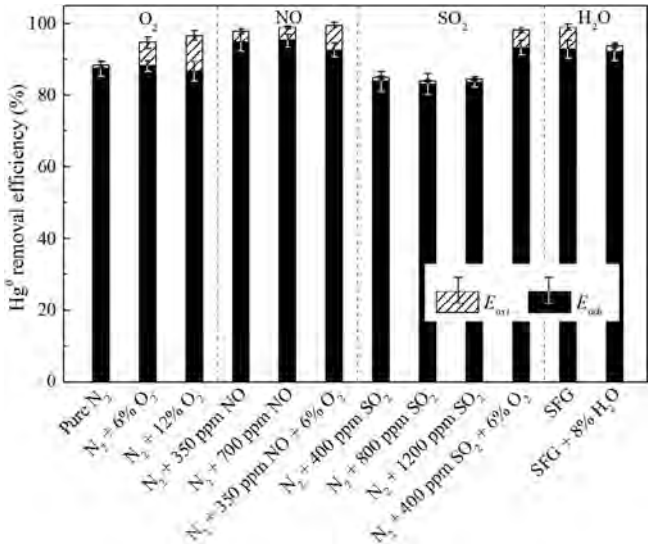

Fig. 8. The effects of gas components on Hg^0 removal over MoCe0.5/AC at 120 °C. (Note: reaction time 3 h, 100 μg/m^3 Hg^0, SFG = 6% O_2 + 12% CO_2 + 350 ppm NO + 400 ppm SO_2 + N_2, 20 g sample, GHSV 2000 h^{-1}).

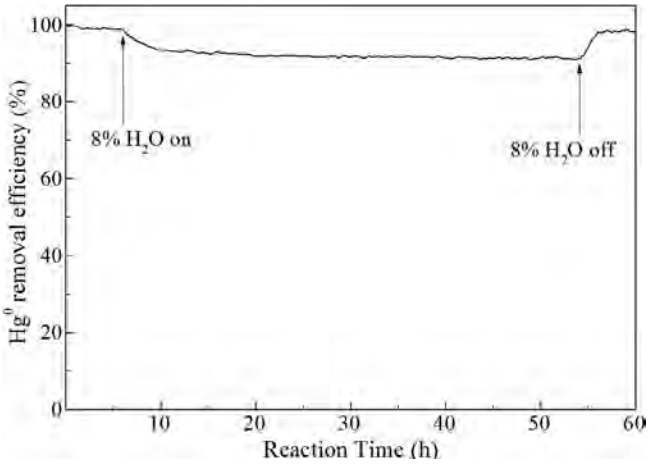

Fig. 9. Stability test of MoCe0.5/AC for Hg^0 removal. (Note: reaction temperature 120 °C, 100 μg/m^3 Hg^0, 6% O_2, 12% CO_2, 350 ppm of NO, 400 ppm of SO_2, 8% H_2O (when used), 20 g sample, GHSV 2000 h^{-1}).

3.3.1. Effect of O_2

As a control group, E_{ads} was 87.46% and E_{oxi} was 0.95% for MoCe0.5/AC at 120 °C under pure N_2 gas flow. The Hg^0 oxidation without O_2 might be attributed to the interaction between the adsorbed mercury and the limited surface active oxygen [18]. After 6% O_2 was added, E_{ads} was 88.27% and E_{oxi} obviously elevated to 6.47%. With the content of O_2 further rising to 12%, E_{ads} reduced to 86.69% while E_{oxi} increased to 9.92%. The cause of the reduction of E_{ads} was likely that a part of adsorbed mercury was oxidized into Hg^{2+} and then released into the gas, which was verified by the enhancement of E_{oxi}. Besides, the increase of E_{oxi} might also be caused by that the consumed lattice oxygen and chemisorbed oxygen could be regenerated by gas-phase oxygen during the Hg^0 removal process [50]. It indicated that O_2 was beneficial to Hg^0 removal and participated in the adsorption and oxidation of Hg^0.

3.3.2. Effect of NO

NO revealed the positive impact for Hg^0 removal regardless of with or without O_2. When 350 ppm and 700 ppm of NO presented, 94.78% and 95.23% of E_{ads} and 3.02% and 3.74% of E_{oxi} were reached, respectively. It might stem from that the potentiation of NO_x, formed from the oxidation of NO, might overmatch the inhibition of the competition surface active sites by NO [20,36]. Furthermore, Hg^0 was nearly purified entirely (E_{rem} = 99.60%) when 6% O_2 was introduced into the 350 ppm of NO, suggesting O_2 could oxidize more NO to form active NO_x species and replenish the consumed surface oxygen [35].

3.3.3. Effect of SO_2

SO_2 restrained the Hg^0 removal in pure N_2 while promoted it in O_2 and N_2. With 1200 ppm of SO_2 balanced in N_2, E_{ads} and E_{oxi} decreased to 83.70% and 0.74% compared with the pure N_2. The suppression phenomenon of SO_2 might be ascribed into two aspects. On the one side, SO_2 could preferentially occupy the adsorption sites than Hg^0, hindering the adsorption and the subsequent oxidation of Hg^0. On the other side, the formed sulfates could cover the surface active oxygen over the sample, which not only interdicted the active sites for Hg^0 removal but also reduced the BET surface area of the sulfated samples S-MoCe0.5/AC and OS-MoCe0.5/AC (Table 2) [17,36].

Moreover, E_{ads} apparently rose to 93.25% and E_{oxi} fell to 4.93% when 400 ppm of SO_2 was added into 6% O_2 and N_2. In addition, OS-MoCe0.5/AC had the lowest BET surface area, which might manifest that the reaction between SO_2 and O_2 formed more sulfates over the surface of MoCe0.5/AC to worsen the BET surface area. In the case, the impairment of the Hg^0 oxidation might be caused by the coverage of the active sites by sulfates, while the increase of Hg^0 adsorption could be related to the formation of more $HgSO_4$ than when O_2 absented [51].

3.3.4. Effect of H_2O

Water vapor commonly exists in the realistic flue gas and has a significant impact on Hg^0 removal. When 8% H_2O was added into the SFG, E_{rem} decreased from 99.04% to 93.71%, which might cause by the competitive adsorption on active sites between H_2O and Hg^0 [43]. In addition, the stability of MoCe0.5/AC under wet SFG (added 8% H_2O) was confirmed as presented in Fig. 9. In the initial 6 h, E_{rem} of MoCe0.5/AC was approximately 99% under the dry SFG gas. Thereafter, 8% H_2O was added for the next 48 h, and E_{rem} was markedly decreased in the initial 2 h and then stayed at about 91%. Significantly, E_{rem} recovered to around 98% when H_2O was shut off, indicating that H_2O could compete with Hg^0 for the active sites while had non-destructive inhibition for the performance of the sample [39,50]. Besides, the good resistance to SO_2 and H_2O and the prominent stability of MoCe0.5/AC were testified, which were important in industrial application.

3.4. XPS

To clarify the compositions and valence states of elements over the sample, the XPS spectra of C 1s, O 1s, Mo 3d, Ce 3d, Hg 4f and S 2p were summarized in Fig. 10. As shown in Table 3, the atomic percent of the C 1s line intensity was normalized as 100% to facilitate quantitative comparisons among the samples.

3.4.1. C 1s

The C 1s spectra (Fig. 10(a)) of fresh AC and MoCe0.5/AC samples were performed deconvolution into four kinds of carbon functional groups: C–C/C=C (284.78–284.81 eV), C–O (286.31–286.32 eV), C=O (288.04–288.10 eV) and O–C=O or COOR (289.67–289.92 eV) [52]. The contents of C–O and C=O were decreased by 1.55% and 1.31% from AC to MoCe0.5/AC, owing to the breakage of the bond in the oxygen functional groups during the thermal treatment process [27]. However, the percentage of COO was increased by 1.81% because of nitrate as a precursor for impregnation [53].

For the used MoCe0.5/AC, the reduction of the oxygen-contained groups (C–O, C=O and COO) implied that all of them involved in the Hg^0 oxidation and/or adsorption [54], which might be the primary pathway of Hg^0 removal over AC without metal loading. Besides, more oxygen-contained groups reduced when SO_2 was added, indicating that the part of oxygen-containing functional groups could also bond with

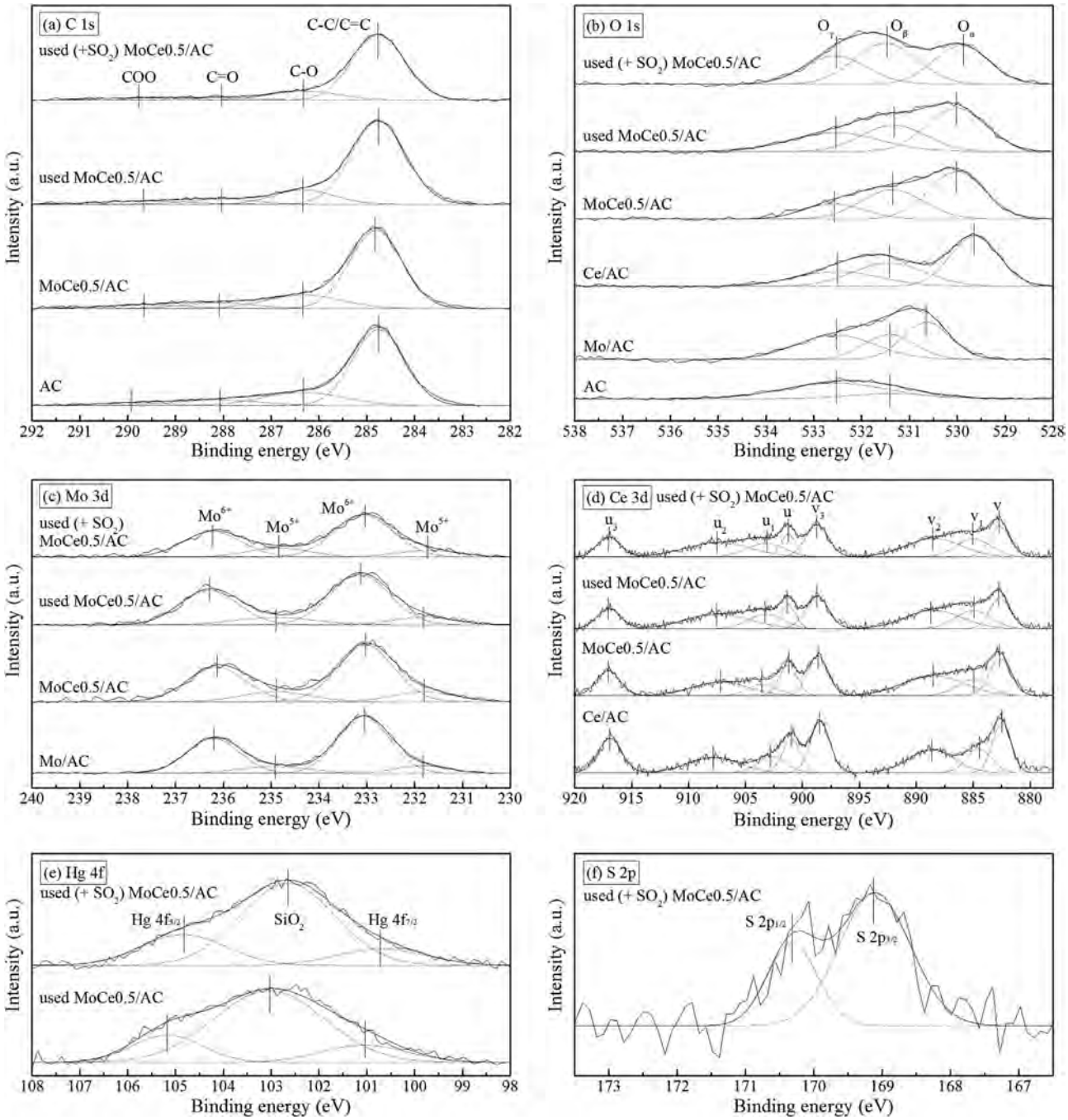

Fig. 10. XPS spectra of fresh and/or used samples over the spectral regions of (a) C 1s, (b) O 1s, (c) Mo 3d, (d) Ce 3d, (e) S 2p and (f) Hg 4f. (Note: reaction time 52 h, reaction temperature 120 °C; "used MoCe0.5/AC": spent by Hg^0 + 6% O_2 + N_2; "used (+ SO_2) MoCe0.5/AC": spent by Hg^0 + 6% O_2 + 400 ppm SO_2 + N_2).

adsorbed SO_2, instead of Hg^0 only.

3.4.2. O 1s

There were two (only for AC) or three sub-peaks for O 1s spectra (Fig. 10(b)). The values of binding energy (BE) at 530 ± 0.50 eV are assigned to lattice oxygen (O_α) in metal oxides, the peaks centered at around 531.40 eV are ascribed to surface chemisorbed oxygen and/or weakly bonded oxygen (O_β), and the peaks at 532.50 ± 0.10 eV are observed to adsorbed water (O_γ) [55]. Obviously, the normalized content of the total O species and O_β for the modified samples were enhanced than AC. It indicated that using metal oxides modifying the active coke could not only add into the lattice oxygen but also increase of the content of surface chemisorbed oxygen. However, the reduction of O_γ for the modified samples, especially for MoCe0.5/AC, might be attributed to the volatilization of adsorbed water during the calcination processes [18]. Moreover, the content of O_α (20.13%) and O_β (13.74%) for MoCe0.5/AC were higher than Mo/AC and Ce/AC, suggesting that the interaction between Mo and Ce oxides could form more surface active oxygen.

For the used MoCe0.5/AC, the contents of O_α and O_β were reduced by 2.74% and 2.27%, respectively, manifesting that both lattice oxygen and chemisorbed oxygen participated in Hg^0 removal. Moreover, for the used (+ SO_2) MoCe0.5/AC, O_α reduced to 16.64%, which might because of the consumption of molybdenum or/and cerium oxygen by SO_2. On the contrary, O_β and O_γ markedly increased to 20.00% and 13.73%, implying that the sulfation not could only introduce an extra

Table 3
The relative XPS intensity normalized to 100% C of as-prepared samples.

Compositions (%)	AC	Mo/AC	Ce/AC	MoCe0.5/AC		
				Fresh	Used	Used (+ SO_2)
Total C 1s	100.00	100.00	100.00	100.00	100.00	100.00
C–C/C=C	69.81	–	–	70.86	75.25	77.86
C–O	18.74	–	–	17.19	14.12	13.93
C=O	8.07	–	–	6.76	5.71	4.02
COO	3.38	–	–	5.19	4.92	4.19
Total O 1s	12.79	24.19	43.61	40.57	40.22	50.38
O_α	–	8.53	19.85	20.13	17.39	16.64
O_β	2.55	6.22	13.70	13.74	11.47	20.00
O_γ	10.24	9.44	10.06	6.70	11.36	13.73
Mo^{6+}/Mo^{5+}	–	5.45	–	4.09	4.83	4.02
Ce^{4+}/Ce^{3+}	–	–	4.94	5.41	3.73	3.65
Mo/Ce ratio	–	–	–	0.62	0.58	0.50

component of O in sulfate, but also increase the content of surface chemisorbed water which might by the reaction of $SO_2 + 2{\cdot}OH \rightarrow SO_3^{2-} + H_2O$ [56,57].

3.4.3. Mo 3d and Ce 3d

The XPS spectra for Mo 3d of Mo/AC and MoCe0.5/AC samples were displayed in Fig. 10(c). The Mo $3d_{5/2}$ and Mo $3d_{3/2}$ fixed deconvolution splitting parameter is 3.1 eV and intensity ration is 0.67 [58]. The BE at 233.03–233.14 eV and 236.13–236.24 eV are Mo^{6+}, while 231.74–231.84 eV and 234.84–234.94 eV are Mo^{5+} [59]. As shown in Fig. 10(d), the characteristic peaks labeled u_1 and v_1 are ascribed to Ce^{3+}, and the other six peaks are attributed to Ce^{4+} [48]. It is noteworthy that the Mo^{6+}/Mo^{5+} ratio diminished from 5.45 for Mo/AC to 4.09 for MoCe0.5/AC, with the typical peaks of Mo 3d gently shifted to the lower BE [60]. However, the Ce^{4+}/Ce^{3+} ratio enhanced from 4.94 for Ce/AC to 5.41 for MoCe0.5/AC. These changes indicated that the redox reaction between Mo and Ce species existed over the MoCe0.5/AC, where Mo^{6+} could oxidize Ce^{3+} and generate Ce^{4+} ($Mo^{6+} + Ce^{3+} \rightarrow Mo^{5+} + Ce^{4+}$). The redox reaction between Mo and Ce species could not only maintain the Ce^{4+} providing for Hg^0 oxidation and adsorption but also promote the redox shift between Ce^{4+} and Ce^{3+}, which would be helpful to the high Hg^0 removal performance and the prominent stability of MoCe0.5/AC [61].

For the used MoCe0.5/AC, Ce^{4+}/Ce^{3+} ratio declined to 3.73, demonstrating that Ce^{4+} was reduced to Ce^{3+} during the Hg^0 removal process and contributed to Hg^0 oxidation. At the same time, the content of Mo^{6+} increased, which might owe to Mo^{5+} was re-oxidized to Mo^{6+} by oxygen gas or adsorbed oxygen species. Noticeably, when introducing SO_2, the Mo^{6+}/Mo^{5+} ratio was reduced by 0.81 and the Ce^{4+}/Ce^{3+} ratio was slightly decreased, as well as the Mo/Ce atomic ratio diminished from 0.58 to 0.50 (Table 3). These results were similar to the report of Kwon et al. [38]. It might infer that the SO_2 mainly combined with MoO_3 instead of CeO_2, and then formed sulfate. Thereby, the high valence of Ce over the MoCe0.5/AC could be protected and used for Hg^0 removal, which means that Mo^{6+} played a significant role in SO_2 resistance.

3.4.4. Hg 4f and S 2p

For the used MoCe0.5/AC samples, the XPS peaks of Hg 4f (Fig. 10(e)) at 100.71–101.06 eV and 104.83–105.18 eV corresponded to the Hg $4f_{7/2}$ and Hg $4f_{5/2}$ (both for Hg^{2+}), respectively [62]. The high intensity peaks at 102.66 eV and 103.04 eV were Si 2p for SiO_2 [43]. However, there was no peak for Hg^0 whether or not SO_2 existing during the reaction, suggesting that the physically adsorbed Hg^0 was narrow or/and had been desorbed from the sample [28]. Therefore, the major mercury species on the surface of the used MoCe0.5/AC samples was HgO. Furthermore, for the used (+ SO_2) MoCe0.5/AC, the Hg 4f peaks shifted to lower BE and two S 2p peaks (Fig. 10(f)) at 170.31 eV (S $2p_{1/2}$) and 169.11 eV (S $2p_{3/2}$) both assigned to SO_4^{2-} and metal sulfates [9], speculating that a part of mercuric oxide might react with sulfide and form to $HgSO_4$ [44]. The formation of mercury species over the spent samples was discussed in the following Hg-TPD tests.

3.5. Adsorbed mercury species

A range of adsorbed samples was treated by Hg-TPD to verify the mercury removal mechanism. The relevant results of Hg-TPD tests and its optimum fitting profiles were recorded in Table 4 and Fig. 11. The mercury mass balance ratio (B_{Hg}) between the Hg^0 removal test and Hg-TPD test closed to 100%, implying that almost all of the adsorbed mercury compounds on the sorbents were decomposed into Hg^0 during the thermal treatment. Moreover, the loss B_{Hg} was within the range of experimental permissible error [42,54].

According to the results, there was a low concentration of gaseous Hg^{2+} for the Hg^0 removal test and a tiny signal of physically adsorbed Hg^0 in the Hg-TPD test. It could further verify that the chemisorption of Hg^0 was the primary way to remove Hg^0, while catalytic oxidation and physisorption of Hg^0 only played a small role, which was in line with the results of Fig. 8 and XPS. Furthermore, the temperature of decomposition peak had an ignorable deviation, which was affected by the type of sorbent (AC and MoCe0.5/AC) and/or the reaction gas compositions (O_2 and SO_2). Moreover, the variation of Hg-TPD fitting peaks area corresponded to the variation of content of chemisorbed mercury species, which could provide an evidence to verify the Hg^0 removal mechanism.

3.5.1. Effect of Mo-Ce oxides

To investigate the effect of Mo-Ce oxides, the Hg-TPD results of used AC and MoCe0.5/AC were contrasted. The gas compositions for Hg^0 removal test was 6% O_2 and N_2. The Hg-TPD profile of AC was fitted into two peaks: peak I and peak II. The two peaks also appeared in decomposition peaks of used MoCe0.5/AC samples, which might be connected with activated coke because of the common character between AC and MoCe0.5/AC. Moreover, combined with the result of XPS, the oxygen-contained groups (C–O, C=O and COO) over the activated coke had involved in the Hg^0 removal, which indicated that the peak I and peak II were likely related to the oxygen functional groups of the activated coke [27,42]. Furthermore, the higher decomposition

Table 4
The relevant results of Hg-TPD profiles and its optimum fitting.

Adsorbed samples	Q_R (μg)	E_{oxi} (%)	Desorbed Hg^0 by Hg-TPD test (μg)					B_{Hg} (%)
			Phy.	I	II	III	IV	
AC-N_2 + O_2	12.01	–	0.03	4.15	7.85	–	–	100.17
M-N_2 + O_2	21.37	5.64	0.02	4.32	7.82	7.22	–	98.49
M-N_2	16.78	0.85	0.02	3.71	7.62	4.67	–	96.94
M-N_2 + O_2 + SO_2	23.41	4.03	0.01	7.94	4.86	5.26	3.89	98.91
M-N_2 + SO_2	15.31	0.26	0.01	5.80	3.59	3.54	1.93	97.62

Note: “M” means the “MoCe0.5/AC” sample; “Phy.” means the physically adsorbed Hg^0 (μg).

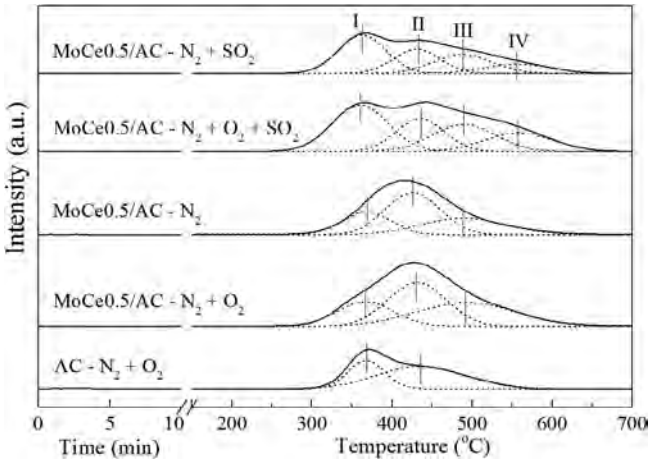

Fig. 11. Hg-TPD profiles of different used AC and MoCe0.5/AC samples. (Note: reaction time 5 h, reaction temperature 120 °C, 200 μg/m^3 Hg^0, 6% O_2 (when used), 400 ppm of SO_2 (when used), 10 g sample, GHSV 4000 h^{-1}; 10 °C/min heating rate for Hg-TPD test).

temperature indicated the stronger bond energy between mercury and adsorption sites, which is a positive correlation [16]. Therefore, the low-temperature peak I approximately at 365 °C could be regarded as the decomposition of weakly adsorbed HgO (weakly-HgO), and the high-temperature peak II at about 430 °C could be ascribed to the strongly bond HgO (strongly-HgO) [63]. However, for the MoCe0.5/AC, apart from the peak I and II, a new peak appeared at around 490 °C and labeled as peak III. Surprisingly, in combination with the XPS results (Fig. 10), both of the peak III and lattice oxygen disappeared on the AC but appeared on the MoCe0.5/AC, namely, there was a coexistence relationship between the peak III and O_α, suggesting that the chemisorbed mercury compound of peak III might be connected with O_α and denoted as O_α-HgO.

Compared with AC, both of the E_{oxi} and the content of O_α-HgO obviously increased over the MoCe0.5/AC, meanwhile a few increments of weakly-HgO and a slight decrease of strongly-HgO could be neglected, manifesting that the mainly effect of Mo-Ce oxides loading was beneficial to Hg^0 oxidation and the O_α-HgO formation.

3.5.2. Effects of O_2 and SO_2

The effects of O_2 and SO_2 for Hg^0 removal mechanism were discussed by changing the gas components of Hg^0 removal test. Meanwhile, the reasons for the SO_2 resistance of MoCe0.5/AC were investigated as well. The peak IV within the Hg-TPD fitting peaks only appeared after samples was treated by SO_2. Based on the result of S 2p in XPS (Fig. 10(f)) and the decomposition temperature at about 545 °C, the mercury compound of peak IV could be deemed to $HgSO_4$ [64].

The result of Hg-TPD had a number of important differences between with or without O_2 for Hg^0 removal. Compared with the pure N_2, both of the Hg^0 oxidation efficiency and the contents of various chemisorbed mercury species were enhanced when O_2 was added. In detail, the amount of Hg^0 removal (Q_R) was increased by 4.59 μg, among them the increment of O_α-HgO supported the largest share as 2.55 μg, implying that more than half of the increment could be identified as the strengthening of O_α-HgO. These findings indicated that the addition of oxygen gas might replenish the consumed chemisorbed oxygen and lattice oxygen, which caused the promotion of Hg^0 oxidation and chemisorption. Moreover, the content of $HgSO_4$ was increased by 1.96 μg when O_2 was added into N_2 + SO_2, verifying that the reaction between O_2 and SO_2 could produce more sulfates and further form $HgSO_4$, which confirmed the conjecture in section 3.3.3.

After SO_2 was injected into pure N_2 or N_2 + O_2, the contents of weakly-HgO and $HgSO_4$ were increased, whereas the strongly-HgO and O_α-HgO were reduced. Based on the results of XPS, BET and Hg-TPD,

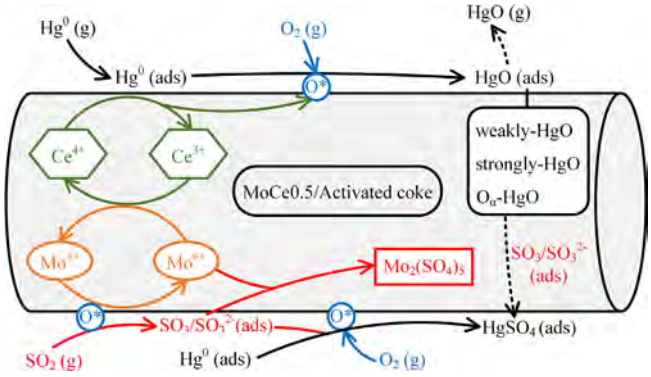

Fig. 12. The proposed mechanism of Hg^0 removal process over MoCe0.5/AC.

the increments of weakly-HgO and $HgSO_4$ might be related to the enhancement of the O_β (Table 3) and the formation of the sulfate, while the restrictions of strongly-HgO and O_α-HgO might be connected with the damage of the surface structure (Table 2) and the consumption of lattice oxygen (Table 3) [13,51,63]. However, the effect of SO_2 to overall Hg^0 removal efficiency was inconsistent between with or without O_2, in which Q_R was decreased by 1.47 μg when O_2 absented, while it was increased by 2.04 μg when O_2 existed. The results suggested that the coexistence of SO_2 and O_2 could further increase the formations of weakly-HgO and $HgSO_4$ and overcome the decreases of strongly-HgO and O_α-HgO. In general, the SO_2 resistance of MoCe0.5/AC could be attributed to the following aspects: (i) the preferential combination between MoO_3 and sulfate could maintain the high valence of Ce for removal of Hg^0; (ii) the coexistence of SO_2 and O_2 could form more weakly-HgO and $HgSO_4$ to enhance the Hg^0 removal.

3.6. Mechanism discussion

From the obtained results and previous researches [55,65], the mechanism for Hg^0 removal over MoCe0.5/AC without HCl (shown in Fig. 12) fits well with the Mars-Maessen mechanism. Firstly, the gaseous elemental mercury could easily be captured by MoCe0.5/AC that possessed special petal-like outer microstructure, large BET surface area and abundant surface active sites. Then, the adsorbed Hg^0 would react with surface active oxygen (denoted as O^*, including chemisorbed oxygen and lattice oxygen), which could be replenished by gaseous O_2, and transformed into HgO. Besides, coupled with the results of XPS, the Ce^{4+}/Ce^{3+} redox couple and the redox reaction between Mo^{6+} and Ce^{3+} might contribute to more O^* for Hg^0 oxidation and adsorption. In summary, detailed reactions for removal of Hg^0 over MoCe0.5/AC could be approximately described as follows [6,66]:

$$Hg^0(g) + \text{sorbent surface} \rightarrow Hg^0(ads) \quad (5)$$

$$Hg^0(ads) + O^* \rightarrow HgO(ads) \quad (6)$$

$$HgO(ads) \rightarrow HgO(g) \quad (7)$$

$$2CeO_2 \rightarrow Ce_2O_3 + O_\alpha \quad (8)$$

$$2MoO_3 + Ce_2O_3 \rightarrow Mo_2O_5 + 2CeO_2 \quad (9)$$

$$Mo^{5+} + O^* \rightarrow Mo^{6+} \quad (10)$$

$$O_2 \rightarrow 2O^* \quad (11)$$

Furthermore, some possible reactions involving in SO_2 were explored and illustrated as the following Eqs. (12)–(15). The absorbed SO_2 was oxidized into SO_3 by O^* and then reacted with absorbed Hg^0 or HgO to form $HgSO_4$, which could give rise to the promotion of Hg^0 chemisorption [13,49]. In addition, O_2 could further facilitate the production of SO_4^{2-} by replenishing of the O^*. Based on the shifts of Mo 3d and Ce 3d XPS spectra, it was certain that the sulfate was largely

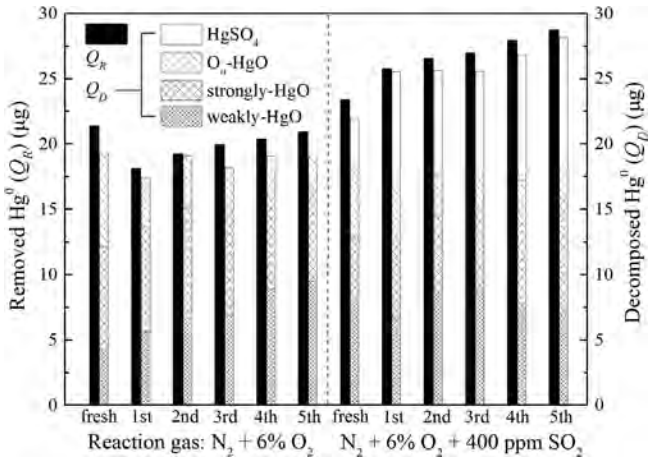

Fig. 13. The amount of removed and desorbed Hg^0 of MoCe0.5/AC over five removal-regeneration cycles. (Note: reaction time 5 h, reaction temperature 120 °C, 200 μg/m^3 Hg^0, 10 g sample, GHSV 4000 h^{-1}; regeneration condition: 10 °C/min, from 150 °C to 700 °C, 500 mL/min pure N_2).

stored in MoO_3 rather than CeO_2 for MoCe0.5/AC sorbent. Therefore, the decrease of O_α-Hg depended not only on the reduction of O_α by sulfating but also on the direct reaction between HgO and SO_3.

$$SO_2\ (ad) + O^* \rightarrow SO_3\ (ad) \quad (12)$$

$$Hg^0(ad) + O^* + SO_3\ (ad) \rightarrow HgSO_4\ (ad) \quad (13)$$

$$HgO\,(ad) + SO_3\ (ad) \rightarrow HgSO_4\ (ad) \quad (14)$$

$$2MoO_3 + 5SO_3\ (ad) \rightarrow Mo_2(SO_4)_5\ (ad) + O^* \quad (15)$$

3.7. Sorbents regeneration

To investigate the regenerability of MoCe0.5/AC, the Hg^0 removal property and the adsorbed mercury species of the regenerated samples were tested. As the results shown in Fig. 13, the amount of decomposed Hg^0 (Q_D) was nearly equivalent to Q_R, and the different might be attributed to the escape of Hg^{2+} during Hg^0 oxidation process. The results suggested that almost all of the adsorbed mercury had been decomposed from the used sample by thermal treatment, and sorbent regeneration process had been finished by Hg-TPD test.

For the reaction without SO_2, Q_R reduced at first and then gradually increased from the 1st to the 5th regeneration cycles. From the result of Q_D, the reduction of performance for regenerated MoCe0.5/AC was principally owing to the decrease of O_α-HgO, as the thermally induced the reduction of lattice oxygen could be triggered at high temperature [17]. However, the weakly-HgO and strongly-HgO were increased from the 1st to the 5th regeneration cycles, which might be concerned with the regenerated character of coal-derived activated coke [21]. Surprisingly, when SO_2 was added into the reaction gas, the mass of mercury adsorption especially $HgSO_4$ and strongly-HgO enhanced with the increased of the regeneration cycles, indicating MoCe0.5/AC possessed high SO_2 tolerance and regenerability. Moreover, to further discussion of the regeneration performance and mechanism, the detailed researches for the effects of regeneration conditions are currently underway.

4. Conclusions

In this paper, Hg^0 removal performance of MoCeY/AC samples prepared by impregnation was measured. In particular, MoCe0.5/AC showed the highest E_{rem} of 94.74% at 120 °C and excellent stability during 48 h test. O_2 and NO were beneficial to the removal of Hg^0, whereas H_2O was an obstacle due to the competitive adsorption of active sites with mercury; the Hg^0 removal was restrained with SO_2 balanced in pure N_2 but be promoted when SO_2 and O_2 coexisted. According to the characterization results, the optimum sample MoCe0.5/AC owned special microstructure, large BET surface area, well-dispersed metal oxides and high reducibility, which promoted the removal of Hg^0. Moreover, the synergistic effect between Mo and Ce oxides ($Mo^{6+} + Ce^{3+} \rightarrow Mo^{5+} + Ce^{4+}$) was verified over the surface of MoCe0.5/AC, which played a significant role in Hg^0 removal as well. According to the Hg-TPD tests, the removal of Hg^0 was mainly done through chemisorption, with a fraction by physisorption and catalytic oxidation. Furthermore, the chemisorbed mercury could be distinguished into weakly-HgO, strongly-HgO, O_α-HgO and $HgSO_4$ (when SO_2 was added). The modified activated coke MoCe0.5/AC possessed the higher oxidation performance than raw AC and could form O_α-HgO. The oxygen gas could replenish the chemisorbed oxygen and lattice oxygen, as E_{oxi} and all of the four chemisorbed mercury species especially O_α-HgO were enhanced after O_2 was added. The high SO_2 resistance of MoCe0.5/AC was resulted from that SO_2 promoted the formations of weakly-HgO and $HgSO_4$, and sulfate was preferentially combined with MoO_3 while CeO_2 could be protected to facilitate Hg^0 removal. Besides, MoCe0.5/AC also showed remarkable regenerability, and it was regarded as a promising sorbent for Hg^0 removal at low temperature especially from the low-rank coal combustion flue gas. Further investigation of the mechanism for regeneration is planned.

Acknowledgments

This work was supported by the National Key Research and Development Program of China [grant number 2016YFC0204100].

References

[1] P.B. Tchounwou, W.K. Ayensu, N. Ninashvili, D. Sutton, Environmental exposure to mercury and its toxicopathologic implications for public health, Environ. Toxicol. 18 (2003) 149–175, https://doi.org/10.1002/tox.10116.
[2] United Nations Environment Programme (UNEP): Minamata Convention on Mercury, UNEP 2013 Minamata, Japan.
[3] U.S.E.I. Administration, International Energy Outlook 2018. https://www.eia.gov/outlooks/ieo/, 2018 (accessed 20 February 2019).
[4] D.G. Streets, Z. Lu, L. Levin, A.F.H. Ter Schure, E.M. Sunderland, Historical releases of mercury to air, land, and water from coal combustion, Sci. Total Environ. 615 (2018) 131–140, https://doi.org/10.1016/j.scitotenv.2017.09.207.
[5] D.G. Streets, H.M. Horowitz, D.J. Jacob, Z. Lu, L. Levin, A.F.H. Ter Schure, E.M. Sunderland, Total mercury released to the environment by human activities, Environ. Sci. Technol. 51 (2017) 5969–5977, https://doi.org/10.1021/acs.est.7b00451.
[6] A.A. Presto, E.J. Granite, Survey of catalysts for oxidation of mercury in flue gas, Environ. Sci. Technol. 40 (2006) 5601–5609, https://doi.org/10.1021/es060504i.
[7] K.C. Galbreath, C.J. Zygarlicke, Mercury speciation in coal combustion and gasification flue gases, Environ. Sci. Technol. 30 (1996) 2421–2426, https://doi.org/10.1021/es950935t.
[8] J.W. Zeng, C.T. Li, L.K. Zhao, L. Gao, X.Y. Du, J. Zhang, L. Tang, G.M. Zeng, Removal of Elemental mercury from simulated flue gas over peanut shells carbon loaded with iodine ions, manganese oxides, and zirconium dioxide, Energy Fuels 31 (2017) 13909–13920, https://doi.org/10.1021/acs.energyfuels.7b02500.
[9] B. Galloway, M. Royko, E. Sasmaz, B. Padak, Mercury oxidation over Cu-SSZ-13 catalysts under flue gas conditions, Chem. Eng. J. 336 (2018) 253–262, https://doi.org/10.1016/j.cej.2017.11.163.
[10] Z.J. Zhou, X.W. Liu, B. Zhao, H.Z. Shao, Y.S. Xu, M.H. Xu, Elemental mercury oxidation over manganese-based perovskite-type catalyst at low temperature, Chem. Eng. J. 288 (2016) 701–710, https://doi.org/10.1016/j.cej.2015.12.057.
[11] H.Z. Shen, I.R. Ie, C.S. Yuan, C.H. Hung, The enhancement of photo-oxidation efficiency of elemental mercury by immobilized WO_3/TiO_2 at high temperatures, Appl. Catal. B: Environ. 195 (2016) 90–103, https://doi.org/10.1016/j.apcatb.2016.04.045.
[12] S. Sjostrom, M. Durham, C.J. Bustard, C. Martin, Activated carbon injection for mercury control: overview, Fuel 89 (2010) 1320–1322, https://doi.org/10.1016/j.fuel.2009.11.016.
[13] H.Y. Wu, C.T. Li, L.K. Zhao, J. Zhang, G.M. Zeng, Y.E. Xie, X.N. Zhang, Y. Wang, Removal of gaseous elemental mercury by cylindrical activated coke loaded with CoO_X-CeO_2 from simulated coal combustion flue gas, Energy Fuels 29 (2015) 6747–6757, https://doi.org/10.1021/acs.energyfuels.5b00871.
[14] L. Gao, C.T. Li, P. Lu, J. Zhang, X.Y. Du, S.H. Li, L. Tang, J.Q. Chen, G.M. Zeng, Simultaneous removal of Hg^0 and NO from simulated flue gas over columnar activated coke granules loaded with La_2O_3-CeO_2 at low temperature, Fuel 215 (2018) 30–39, https://doi.org/10.1016/j.fuel.2017.11.008.

[15] B. Zhao, H.H. Yi, X.L. Tang, Q. Li, D.D. Liu, F.Y. Gao, Copper modified activated coke for mercury removal from coal-fired flue gas, Chem. Eng. J. 286 (2016) 585–593, https://doi.org/10.1016/j.cej.2015.10.107.

[16] H. Xu, Z. Qu, C. Zong, W. Huang, F. Quan, N. Yan, MnO_X/graphene for the catalytic oxidation and adsorption of elemental mercury, Environ. Sci. Technol. 49 (2015) 6823–6830, https://doi.org/10.1021/es505978n.

[17] T. Yao, Y. Duan, C. Zhu, Q. Zhou, J. Xu, M. Liu, H. Wei, Investigation of mercury adsorption and cyclic mercury retention over MnO_X/gamma-Al_2O_3 sorbent, Chemosphere 202 (2018) 358–365, https://doi.org/10.1016/j.chemosphere.2018.03.130.

[18] C. He, B. Shen, J. Chen, J. Cai, Adsorption and oxidation of elemental mercury over Ce-MnO_X/Ti-PILCs, Environ. Sci. Technol. 48 (2014) 7891–7898, https://doi.org/10.1021/es5007719.

[19] Z.J. Zhou, X.W. Liu, J. Xu, X.E. Cao, X.B. Zhu, Elemental mercury removal over a novel starch-modified MnOx/bentonite composite, Fuel Process. Technol. 187 (2019) 16–20, https://doi.org/10.1016/j.fuproc.2019.01.006.

[20] Y.E. Xie, C.T. Li, L.K. Zhao, J. Zhang, G.M. Zeng, X.N. Zhang, W. Zhang, S.S. Tao, Experimental study on Hg^0 removal from flue gas over columnar MnO_X-CeO_2/activated coke, Appl. Surf. Sci. 333 (2015) 59–67, https://doi.org/10.1016/j.apsusc.2015.01.234.

[21] L. Yang, X. Jiang, W.J. Jiang, P.C. Wang, Y. Jin, Cyclic regeneration of pyrolusite-modified activated coke by blending method for flue gas desulfurization, Energy Fuels 31 (2017) 4556–4564, https://doi.org/10.1021/acs.energyfuels.7b00125.

[22] X.Y. Hua, J.S. Zhou, Q.K. Li, Z.Y. Luo, K.F. Cen, Gas-phase elemental mercury removal by ceo_2 impregnated activated coke, Energy Fuels 24 (2010) 5426–5431, https://doi.org/10.1021/ef100554t.

[23] J.F. Ma, C.T. Li, L.K. Zhao, J. Zhang, J.K. Song, G.M. Zeng, X.N. Zhang, Y. Xie, Study on removal of elemental mercury from simulated flue gas over activated coke treated by acid, Appl. Surf. Sci. 329 (2015) 292–300, https://doi.org/10.1016/j.apsusc.2014.11.090.

[24] H.H. Li, Y. Wang, S.K. Wang, X. Wang, J.J. Hu, Promotional effect of Mo addition on CoO_X/Ti-Ce catalyst for oxidation removal of elemental mercury in flue gas, Fuel 224 (2018) 424–433, https://doi.org/10.1016/j.fuel.2018.03.122.

[25] S.J. Yang, Y.F. Guo, N.Q. Yan, D.Q. Wu, H.P. He, J.K. Xie, Z. Qu, J.P. Jia, Remarkable effect of the incorporation of titanium on the catalytic activity and SO_2 poisoning resistance of magnetic Mn-Fe spinel for elemental mercury capture, Appl. Catal. B: Environ. 101 (2011) 698–708, https://doi.org/10.1016/j.apcatb.2010.11.012.

[26] P. Lu, R. Li, Y. Xing, Y.R. Li, T.Y. Zhu, H.F. Yue, W.R. Wu, Low temperature selective catalytic reduction of NO_X with NH_3 by activated coke loaded with $Fe_xCo_yCe_zO_m$: the enhanced activity, mechanism and kinetics, Fuel 233 (2018) 188–199, https://doi.org/10.1016/j.fuel.2018.05.076.

[27] X.Y. Du, C.T. Li, L.K. Zhao, J. Zhang, L. Gao, J.J. Sheng, Y.Y. Yi, J.Q. Chen, G.M. Zeng, Promotional removal of HCHO from simulated flue gas over Mn-Fe oxides modified activated coke, Appl. Catal. B: Environ. 232 (2018) 37–48, https://doi.org/10.1016/j.apcatb.2018.03.034.

[28] J.Q. Chen, C.T. Li, S.H. Li, P. Lu, L. Gao, X.Y. Du, Y.Y. Yi, Simultaneous removal of HCHO and elemental mercury from flue gas over Co-Ce oxides supported on activated coke impregnated by sulfuric acid, Chem. Eng. J. 338 (2018) 358–368, https://doi.org/10.1016/j.cej.2018.01.043.

[29] S.S. Tao, C.T. Li, X.P. Fan, G.M. Zeng, P. Lu, X. Zhang, Q.B. Wen, W.W. Zhao, D.Q. Luo, C.Z. Fan, Activated coke impregnated with cerium chloride used for elemental mercury removal from simulated flue gas, Chem. Eng. J. 210 (2012) 547–556, https://doi.org/10.1016/j.cej.2012.09.028.

[30] H. Xu, Y. Ma, W. Huang, J. Mei, S. Zhao, Z. Qu, N. Yan, Stabilization of mercury over Mn-based oxides: speciation and reactivity by temperature programmed desorption analysis, J. Hazard. Mater. 321 (2017) 745–752, https://doi.org/10.1016/j.jhazmat.2016.09.030.

[31] W. Yang, Y.X. Liu, Q. Wang, J.F. Pan, Removal of elemental mercury from flue gas using wheat straw chars modified by Mn-Ce mixed oxides with ultrasonic-assisted impregnation, Chem. Eng. J. 326 (2017) 169–181, https://doi.org/10.1016/j.cej.2017.05.106.

[32] Y. Gao, Z. Zhang, J. Wu, L. Duan, A. Umar, L. Sun, Z. Guo, Q. Wang, A critical review on the heterogeneous catalytic oxidation of elemental mercury in flue gases, Environ. Sci. Technol. 47 (2013) 10813–10823, https://doi.org/10.1021/es402495h.

[33] J. Kašpar, P. Fornasiero, M. Graziani, Use of CeO_2-based oxides in the three-way catalysis, Catal. Today 50 (1999) 285–298, https://doi.org/10.1016/s0920-5861(98)00510-0.

[34] T. Montini, M. Melchionna, M. Monai, P. Fornasiero, Fundamentals and catalytic applications of CeO_2-based materials, Chem. Rev. 116 (2016) 5987–6041, https://doi.org/10.1021/acs.chemrev.5b00603.

[35] H. Li, S. Wu, C.Y. Wu, J. Wang, L. Li, K. Shih, SCR atmosphere induced reduction of oxidized mercury over CuO-CeO_2/TiO_2 catalyst, Environ. Sci. Technol. 49 (2015) 7373–7379, https://doi.org/10.1021/acs.est.5b01104.

[36] J. Yang, W. Zhu, S. Zhang, M. Zhang, W. Qu, H. Li, Z. Zeng, Y. Zhao, J. Zhang, Role of flue gas components in Hg^0 oxidation over $La_{0.8}Ce_{0.2}MnO_3$ perovskite catalyst in coal combustion flue gas, Chem. Eng. J. 360 (2019) 1656–1666, https://doi.org/10.1016/j.cej.2018.10.218.

[37] S.O. Omarov, E.A. Vlasov, D.A. Sladkovskiy, K.V. Semikin, A.N. Matveyeva, S.P. Fedorov, G.V. Oganesyan, D.Y. Murzin, Physico-chemical properties of MoO_3/ZrO_2 catalysts prepared by dry mixing for isobutane alkylation and butene transformations, Appl. Catal. B: Environ. 230 (2018) 246–259, https://doi.org/10.1016/j.apcatb.2018.02.020.

[38] D.W. Kwon, K.H. Park, S.C. Hong, Enhancement of SCR activity and SO_2 resistance on VOx/TiO_2 catalyst by addition of molybdenum, Chem. Eng. J. 284 (2016) 315–324, https://doi.org/10.1016/j.cej.2015.08.152.

[39] X.L. Hu, Q. Shi, H. Zhang, P.F. Wang, S.H. Zhan, Y. Li, NH_3-SCR performance improvement over Mo modified Mo(x)-MnO_X nanorods at low temperatures, Catal. Today 297 (2017) 17–26, https://doi.org/10.1016/j.cattod.2017.06.015.

[40] M.A. Lopez-Anton, Y. Yuan, R. Perry, M.M. Maroto-Valer, Analysis of mercury species present during coal combustion by thermal desorption, Fuel 89 (2010) 629–634, https://doi.org/10.1016/j.fuel.2009.08.034.

[41] A. Dandekar, R.T.K. Baker, M.A. Vannice, Characterization of activated carbon, graphitized carbon fibers and synthetic diamond powder using TPD and DRIFTS, Carbon 36 (1998) 1821–1831, https://doi.org/10.1016/s0008-6223(98)00154-7.

[42] P. Sun, B. Zhang, X.B. Zeng, G.Q. Luo, X. Li, H. Yao, C.G. Zheng, Deep study on effects of activated carbon's oxygen functional groups for elemental mercury adsorption using temperature programmed desorption method, Fuel 200 (2017) 100–106, https://doi.org/10.1016/j.fuel.2017.03.031.

[43] J.Y. Zhang, C.T. Li, L.K. Zhao, T. Wang, S.H. Li, G.M. Zeng, A sol-gel Ti-Al-Ce-nanoparticle catalyst for simultaneous removal of NO and Hg^0 from simulated flue gas, Chem. Eng. J. 313 (2017) 1535–1547, https://doi.org/10.1016/j.cej.2016.11.039.

[44] L.K. Zhao, C.T. Li, S.H. Li, Y. Wang, J.Y. Zhang, T. Wang, G.M. Zeng, Simultaneous removal of elemental mercury and NO in simulated flue gas over V_2O_5/ZrO_2-CeO_2 catalyst, Appl. Catal. B: Environ. 198 (2016) 420–430, https://doi.org/10.1016/j.apcatb.2016.05.079.

[45] D.R. Mullins, S.H. Overbury, D.R. Huntley, Electron spectroscopy of single crystal and polycrystalline cerium oxide surfaces, Surf. Sci. 409 (1998) 307–319.

[46] M. Trépanier, A. Tavasoli, A.K. Dalai, N. Abatzoglou, Co, Ru and K loadings effects on the activity and selectivity of carbon nanotubes supported cobalt catalyst in Fischer–Tropsch synthesis, Appl. Catal. A: Gen., 353 (2009) 193–202, https://doi.org/10.1016/j.apcata.2008.10.061.

[47] P. Arnoldy, J.C.M. De Jonge, J.A. Moulijn, Temperature-programmed reduction of MoO_3 and MoO_2, J. Phys. Chem. 89 (1984) 4517–4526, https://doi.org/10.1021/j100267a021.

[48] L.K. Zhao, C.T. Li, X.Y. Du, G.M. Zeng, L. Gao, Y.B. Zhai, T. Wang, J.Y. Zhang, Effect of Co addition on the performance and structure of V/ZrCe catalyst for simultaneous removal of NO and Hg^0 in simulated flue gas, Appl. Surf. Sci. 437 (2018) 390–399, https://doi.org/10.1016/j.apsusc.2017.08.165.

[49] X.P. Fan, C.T. Li, G.M. Zeng, X. Zhang, S.S. Tao, P. Lu, Y. Tan, D.Q. Luo, Hg^0 removal from simulated flue gas over CeO_2/HZSM-5, Energy Fuels 26 (2012) 2082–2089 https://doi.org/.

[50] T. Wang, C.T. Li, L.K. Zhao, J.Y. Zhang, S.H. Li, G.M. Zeng, The catalytic performance and characterization of ZrO_2 support modification on CuO-CeO_2/TiO_2 catalyst for the simultaneous removal of Hg^0 and NO, Appl. Surf. Sci. 400 (2017) 227–237, https://doi.org/10.1016/j.apsusc.2016.12.192.

[51] H.H. Li, S.K. Wang, X. Wang, J.J. Hu, Activity of $CuCl_2$-modified cobalt catalyst supported on Ti-Ce composite for simultaneous catalytic oxidation of Hg^0 and NO in a simulated pre-sco process, Chem. Eng. J. 316 (2017) 1103–1113, https://doi.org/10.1016/j.cej.2017.02.052.

[52] S. Biniak, G. Szymański, J. Siedlewski, A. Świątkowski, The characterization of activated carbons with oxygen and nitrogen surface groups, Carbon 35 (1997) 1799–1810, https://doi.org/10.1016/s0008-6223(97)00096-1.

[53] Y.H. Li, C.W. Lee, B.K. Gullett, Importance of activated carbon's oxygen surface functional groups on elemental mercury adsorption☆, Fuel 82 (2003) 451–457, https://doi.org/10.1016/s0016-2361(02)00307-1.

[54] B. Zhang, P. Xu, Y. Qiu, Q. Yu, J.J. Ma, H. Wu, G.Q. Luo, M.H. Xu, H. Yao, Increasing oxygen functional groups of activated carbon with non-thermal plasma to enhance mercury removal efficiency for flue gases, Chem. Eng. J. 263 (2015) 1–8, https://doi.org/10.1016/j.cej.2014.10.090.

[55] J. Zhou, W. Hou, P. Qi, X. Gao, Z. Luo, K. Cen, CeO_2-TiO_2 sorbents for the removal of elemental mercury from syngas, Environ. Sci. Technol. 47 (2013) 10056–10062, https://doi.org/10.1021/es401681y.

[56] A.C. Zhang, Z.H. Zhang, H. Lu, Z.C. Liu, J. Xiang, C.S. Zhou, W.B. Xing, L.S. Sun, Effect of promotion with ru addition on the activity and SO_2 resistance of MnO_X–TiO_2 adsorbent for Hg^0 removal, Ind. Eng. Chem. Res. 54 (2015) 2930–2939, https://doi.org/10.1021/acs.iecr.5b00211.

[57] Y. Zhao, R. Hao, B. Yuan, J. Jiang, Simultaneous removal of SO_2, NO and Hg^0 through an integrative process utilizing a cost-effective complex oxidant, J. Hazard. Mater. 301 (2016) 74–83, https://doi.org/10.1016/j.jhazmat.2015.08.049.

[58] Y.L. Meng, T. Wang, S. Chen, Y.J. Zhao, X.B. Ma, J.L. Gong, Selective oxidation of methanol to dimethoxymethane on V_2O_5–MoO_3/γ-Al_2O_3 catalysts, Appl. Catal. B: Environ. 160–161 (2014) 161–172, https://doi.org/10.1016/j.apcatb.2014.05.008.

[59] K. Hada, J. Tanabe, S. Omi, M. Nagai, Characterization of cobalt molybdenum nitrides for thiophene HDS by XRD, TEM, and XPS, J. Catal. 207 (2002) 10–22, https://doi.org/10.1006/jcat.2001.3495.

[60] S.J. Zhao, Z. Li, Z. Qu, N.Q. Yan, W.J. Huang, W.M. Chen, H.M. Xu, Co-benefit of Ag and Mo for the catalytic oxidation of elemental mercury, Fuel 158 (2015) 891–897, https://doi.org/10.1016/j.fuel.2015.05.034.

[61] Y. Wang, B. Shen, C. He, S. Yue, F. Wang, Simultaneous Removal of NO and Hg^0 from Flue Gas over Mn-Ce/Ti-PILCs, Environ. Sci. Technol. 49 (2015) 9355–9363, https://doi.org/10.1021/acs.est.5b01435.

[62] N.D. Hutson, B.C. Attwood, K.G. Scheckel, XAS and XPS characterization of mercury binding on brominated activated carbon, Environ. Sci. Technol. 41 (2007) 1747–1752, https://doi.org/10.1021/es062121q.

[63] Q. Wan, L. Duan, K.B. He, J.H. Li, Removal of gaseous elemental mercury over a CeO_2-WO_3/TiO_2 nanocomposite in simulated coal-fired flue gas, Chem. Eng. J. 170 (2011) 512–517, https://doi.org/10.1016/j.cej.2010.11.060.

[64] S.J. Wu, M.A. Uddin, S. Nagano, M. Ozaki, E. Sasaoka, Fundamental study on decomposition characteristics of mercury compounds over solid powder by

temperature-programmed decomposition desorption mass spectrometry, Energy Fuels 25 (2011) 144–153, https://doi.org/10.1021/ef1009499.
[65] E.J. Granite, H.W. Pennline, R.A. Hargis, Novel sorbents for mercury removal from flue gas, Ind. Eng. Chem. Res. 39 (2000) 1020–1029, https://doi.org/10.1021/Ie990758v.
[66] X.N. Zhang, C.T. Li, L.K. Zhao, J. Zhang, G.M. Zeng, Y.E. Xie, M.E. Yu, Simultaneous removal of elemental mercury and NO from flue gas by V_2O_5–CeO_2/TiO_2 catalysts, Appl. Surf. Sci. 347 (2015) 392–400, https://doi.org/10.1016/j.apsusc.2015.04.039.